Composites Part C: Open Access 2 (2020) 100019

Contents lists available at ScienceDirect

Composites Part C: Open Access

journal homepage: www.elsevier.com/locate/jcomc

Anisotropic tensile behaviour of short glass-fibre reinforced polyamide-6

Petter Henrik Holmström [a,b,*], Odd Sture Hopperstad [a,b], Arild Holm Clausen [a,b]

[a] Department of Structural Engineering, Structural Impact Laboratory (SIMLab), Norwegian University of Science and Technology (NTNU), Trondheim, NO 7491, Norway

[b] Centre for Advanced Structural Analysis (CASA), NTNU, Trondheim, NO 7491, Norway

ARTICLE INFO

Keywords:
Polymer-matrix composites (PMCs)
Discontinuous fibres
Polyamide-6
Mechanical properties
Anisotropy
CT analysis

ABSTRACT

This paper presents an experimental investigation of injection-moulded short glass-fibre reinforced polyamide-6 reinforced with 0 wt.%, 15 wt.% and 30 wt.% fibres. The fibre orientation distributions are characterized by use of X-ray computed tomography. A shell-core-shell structure is found through the thickness of the materials, where the predominant fibre orientation is along the mould flow direction (MFD) in the shell layers and perpendicular to the MFD in the core layer. To study the mechanical behaviour, uniaxial tensile tests are conducted in seven directions relative to the MFD. The tests are instrumented with two cameras, which allows for accurate measurement of all strain components. The fibre-reinforced materials show moderate to high degree of anisotropy, increasing with the fibre content. Young's modulus, in-plane and out-of-plane Poisson's ratio, stress at maximum force and fracture strain vary smoothly with the in-plane specimen angle. It is demonstrated that orthotropic elasticity is an excellent approximation for the anisotropic elastic behaviour of the fibre-reinforced materials.

1. Introduction

The present study is limited to short glass-fibre reinforced thermoplastics produced by injection moulding. Injection moulding is an attractive production method which allows for rapid processing, low cost at high production volumes and large flexibility in design geometry, where multiple functions can be integrated in one part. The structural performance of this material class may reach high levels and even challenge the use of metals in load-bearing components. The automotive industry uses short glass-fibre reinforced polymers in structural applications, where examples include engine mounts, intake manifolds, front-end carriers and clutch pedals.

A fibre contributes to stiffness and strength in the direction of its axis, which makes the orientations of the fibres crucial for the mechanical properties of the composite material. The fibre orientations are governed by the melt flow and depend on a number of factors such as mould geometry, injection gate positions, injection speed, barrel temperature, mould temperature, mould thickness, notches, sharp corners and fibre content [1–3]. Furthermore, fibres tend to break during the moulding process, which typically results in Weibull-shaped fibre length distributions with peak between 100 and 600 μm and maximum fibre length below 1–2 mm [2–8]. Today, fibre orientation and length measurements are typically obtained from volumetric X-ray computed tomography (X-CT) images.

Among the large number of publications, there is consensus on a five-layered skin-shell-core-shell-skin structure of fibre orientations through the thickness of a plate [2,6,7,9–18]. Many authors neglect the very thin skin layers, which typically are dominated by randomly oriented fibres, in their representation of the material. Hence, it is common to consider a structure with three layers where the predominant fibre orientation in the core and shells is, respectively, transverse and longitudinal to the mould flow direction (MFD). The fibre content is generally reported to be higher in the core layer than in the shell layers and the relative thickness of each layer depends on the materials (e.g. fibre content) and the processing parameters (e.g. flow speed, viscosity, polymer and mould temperature). The out-of-plane orientation component is generally small in plates, but large values are reported at weld lines and near obstacles such as notches [19–21]. Furthermore, the fibre length and orientation distributions seem to be correlated, where the orientation of shorter fibres is more random than the orientation of longer fibres [3,6].

The shell-core-shell structure of fibre orientations generally makes such materials anisotropic. Material anisotropy is usually examined by off-axis tensile tests, where the off-axis angle is the in-plane rotation (relative to the MFD) of the specimen and pull direction. Previous investigations show that the tensile stiffness and strength tend to decrease as the off-axis angle increases, where similar values are found between 45° and 90° [2,6,9,10,12,14,15,22–24]. When it comes to ductility, the fracture strain is lowest in the 0°-direction and the majority of the studies find that the fracture strain is larger for 45° specimens than for 90° specimens.

* Corresponding author.
E-mail address: petter.h.holmstrom@ntnu.no (P.H. Holmström).

https://doi.org/10.1016/j.jcomc.2020.100019
Received 3 June 2020; Received in revised form 3 July 2020; Accepted 14 August 2020

Limiting the attention to the response in the MFD, Young's modulus increases both with the stiffness of the matrix material and the fibre content, where some studies also find that the increase with the fibre content is linear [25–32]. On the other hand, Young's modulus seems independent of the fibre length as long as the fibres are longer than a critical value [32,33]. The tensile strength in the MFD is reported to increase linearly with the fibre content at low contents and non-linearly at high contents [26–31]. The fibre lengths play a role for the strength, which is found to increase rapidly with the fibre length for short fibres and to approach an asymptotic value for longer fibres [25,27,34]. The fracture strain in the MFD decreases with increasing fibre content [25,26,28,29]. The effect of the fibre diameter on elastic mechanical properties is generally small [35].

Studies on the off-axis behaviour of short fibre-reinforced thermoplastics typically report the stress-strain curves with the corresponding stiffness, strength and fracture strain values, but other aspects are seldom considered. Some improvements of particular interest are to study the response for an increased number of off-axis angles compared with the commonly applied 0°, 45° and 90° directions, to characterize the matrix material to have a reference for the fibre-reinforced material and to apply digital image correlation (DIC) to measure the local deformations. The latter allows for accurate measurements of transverse strains, heterogeneities of the strain fields and localized deformation, which may give valuable insight in the material behaviour. All these topics are addressed in this paper.

Design of load-bearing components made of short glass-fibre reinforced thermoplastics requires not only a thorough understanding of the mechanical behaviour, but also reliable, accurate and efficient material models for use in finite element simulations. Models for this class of materials are either formulated on the macroscopic level, using e.g. orthotropic elasticity, or as micromechanical models, where computations are performed directly on the material phases. A number of promising macroscopic models incorporating anisotropy have been proposed for short glass-fibre reinforced thermoplastics [22,23,36–45]. Micromechanical models usually require information about the fibre content and orientations and the mechanical properties of the fibre and matrix materials. Such information is, however, seldom provided in experimental studies. More high-quality experiments are also needed for validation of representative volume element (RVE) simulations, which have become a very useful approach for studying the material behaviour (see e.g. [46–50]).

The primary objective of this paper is to study the anisotropic material behaviour of injection-moulded short glass-fibre reinforced polyamide-6, using tests properly instrumented for DIC analysis of all strain components. The secondary objective is to generate a test database incorporating information from fibre orientation measurements and uniaxial tension tests of fibre-reinforced and unreinforced material, which may support phenomenological and micromechanical modelling of such materials.

The paper is organized as follows. First, the three materials are presented, namely the unreinforced polyamide-6 (PA) and the short E-glass-fibre reinforced polyamide-6 with 15 wt.% (PA15) and 30 wt.% (PA30) fibres. Second, computed tomography (CT) is applied to determine the probability density functions of the projected fibre angles (henceforth referred to as FODs) for the two glass-fibre reinforced materials. Third, quasi-static tensile tests instrumented with two digital cameras are performed in seven directions for the materials with 15 wt.% and 30 wt.% fibres and three directions for unreinforced polyamide-6. Results are discussed consecutively, while the supplementary material to this article, available through Mendeley Data [51], provides more details of the tensile experiments. The paper is rounded off with conclusions.

2. Materials

All three materials are sold under commercial trade names by a global producer of polymer materials and marketed as suitable for injection moulding, where the polyamide-6 matrix of the three materials is supposed to be the same. The materials were delivered as injection-moulded rectangular plates with nominal measures 200 mm × 140 mm × 3 mm (long, wide and thick).

Table 1
Measured density ρ and fibre weight fraction w_f, and estimated fibre volume fraction v_f.

Material	ρ [kg/m^3]	w_f [–]	v_f [–]
PA	1137	–	–
PA15	1232	0.1366	0.064
PA30	1359	0.2904	0.152

The density ρ and fibre weight fraction w_f were measured by SINTEF Industry (Oslo, Norway) using one single sample extracted near the plate centre. The fibre weight fraction w_f was found by burning off the matrix material under controlled conditions (gradually increasing the temperature to 550° over 300 min and holding at 550° for 30 min). The fibre volume fraction v_f is often a parameter in constitutive models, which may be estimated from

$$v_f = 1 - \frac{\rho}{\rho_m}\left(1 - w_f\right) \tag{1}$$

where ρ_m and ρ are, respectively, the density of the matrix and fibre-reinforced material. A derivation of Eq. (1) is provided in the supplementary material. Results from the measurements and estimations are given in Table 1.

Hygroscopic effects in polyamides substantially influence the mechanical behaviour [52,53] and the water content of the three materials was therefore measured at the time of testing by baking a few dedicated samples in an oven at 80° for 14 days. For all materials, the measured water content was approximately 0.9 wt.%.

3. Characterization of the fibre phase

3.1. Setup

For both PA15 and PA30, one column-shaped specimen with square cross-section was prepared for X-ray computed tomography (X-CT) investigation, as illustrated in Fig. 1(a). The longitudinal direction of the specimen was oriented in the MFD and the width and thickness of the cross-section (approximately 3 mm × 3 mm) were equal to the plate thickness. The column was centred in the transverse direction of the plate and extracted such that the approximately 5 mm long scanned region (coloured yellow in the figure) was located close to the plate centre in the longitudinal direction. A Nikon XT H 225 ST scanner (RECX Laboratory, Department of Physics, NTNU, Norway) with the scan parameters listed in Table 2 was used to acquire the images, where the resulting characteristic voxel size of 2.70 μm is small enough to ensure multiple voxels in the radial direction of the fibres.

The two datasets of projected X-ray images were reconstructed using the software CT Pro 3D (version XT 3.1.3, Nikon Metrology). The Fiber Composite Material Analysis Module in VGStudio MAX 3.0 was applied to calculate the projected fibre angles α, β and γ in the three coordinate planes, defined in Fig. 1, and to construct FODs. The fibre volume fraction was computed with the Advanced Surface Determination tool in VGStudio MAX 3.0, but was underestimated compared to the values provided in Table 1. To account for this, the measured through-thickness variation of fibre volume content was normalized and scaled such that the mean fibre volume fraction corresponds to the values in Table 1.

3.2. Results and discussion

Fig. 2(a) shows the probability density functions of the projected fibre angles (FODs) for the scanned volume of the PA15. A narrow FOD

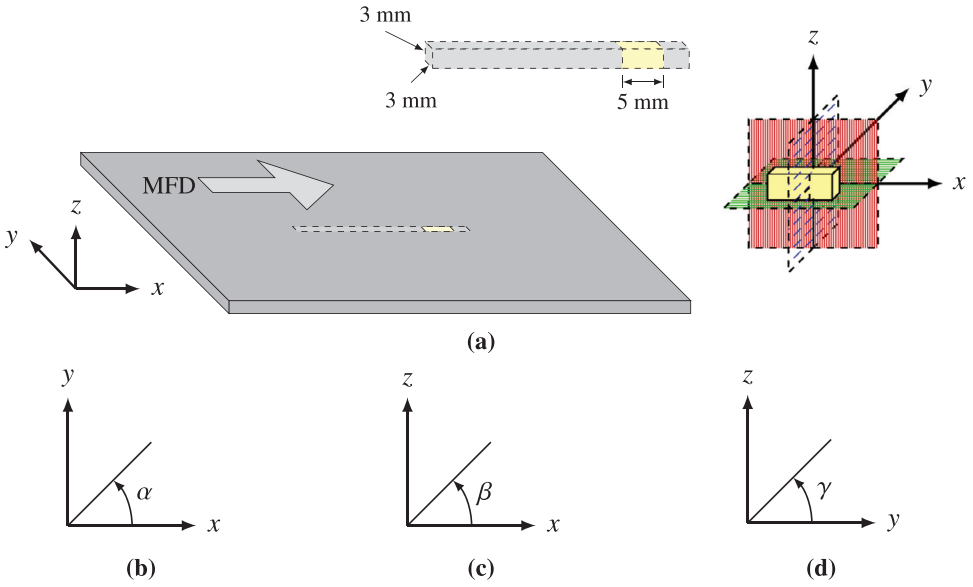

Fig. 1. **(a)** Extraction of column-shaped specimen for X-CT imaging and reference coordinate system for the quantitative fibre analysis, where the yellow region corresponds to the scanned part of the specimen. Projected fibre angles **(b)** α, **(c)** β and **(d)** γ are computed in the *xy*-, *xz*- and *yz*-plane, respectively.

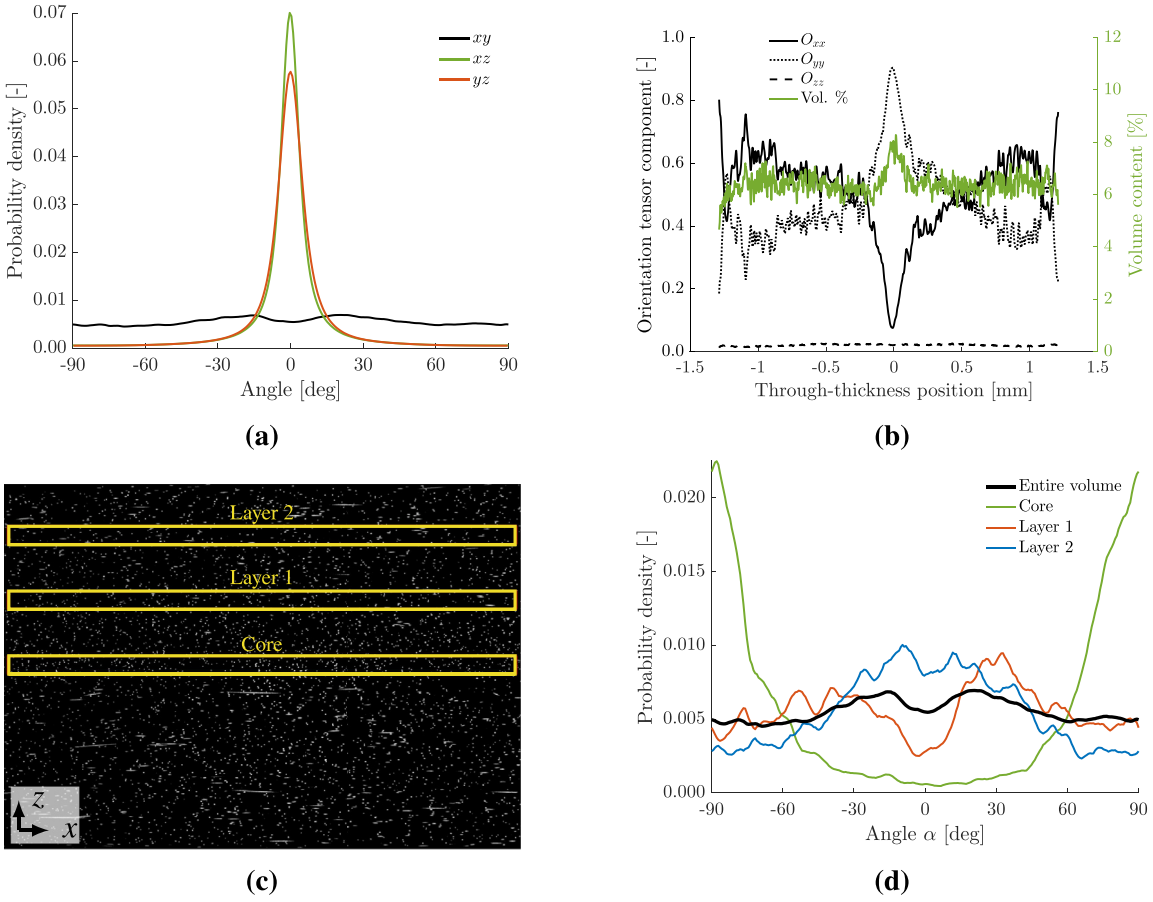

Fig. 2. Quantitative analysis of fibre orientation in PA15. **(a)** Comparison of FODs in the *xy*-, *xz*- and *yz*-plane. **(b)** Orientation tensor components and fibre volume content through the thickness for fibres projected to the *xy*-plane. **(c)** ROIs illustrated in the *xz*-plane. **(d)** FODs in the *xy*-plane for the ROIs.

Table 2
Parameters applied in the X-CT scans.

Voltage [kV]	Current [μA]	Exposure [μs]	Gain [dB]	Proj. angles [–]	Frames per proj. [–]	Magnification [–]	Voxel size [μm]	Target mat. [–]
60	300	2000	24	1500	4	74.08	2.70	Mo

around 0° is found for fibres projected to the *xz*- and *yz*-plane, which implies that the out-of-plane fibre orientation component is generally small. In the *xy*-plane (the plate plane), the FOD is nearly random with minor peaks at ±15°. Fig. 2(b) displays the through-thickness variation of the components of the second-order orientation tensor **O** [54] for PA15, where **O** is constructed such that the diagonal elements represent the degree of alignment in the *x*-, *y*- and *z*-direction, and $O_{xx} + O_{yy} + O_{zz} = 1$. The degree of alignment with the MFD (O_{xx}) is largest near the surfaces and decreases gradually towards the core layer, where the peak of O_{yy} indicates that the probability of fibre alignment perpendicular to the MFD is very high. Defining the core layer thickness as twice the distance from the intersection point of the curves $O_{xx}(z)$ and $O_{yy}(z)$ for negative z to $z = 0$, the core layer of PA15 measures 374 μm, which is 13% of the total thickness. Fig. 2(b) shows also the fibre volume fraction through the thickness, which apparently is nearly constant with a small peak of increased fibre content in the core layer. A final important observation from Fig. 2(b) is that the orientation tensor component O_{zz} is negligible through the entire thickness. Thus, the fibres are in general located in the *xy*-plane, and α is the interesting one of the three angles defined in Fig. 1. FODs in the *xy*-plane are computed for PA15 in the regions of interest (ROIs) illustrated in Fig. 2(c), where each ROI spans over a limited proportion of the thickness and the complete width and length of the scanned sample shown in Fig. 1(a). Fig. 2(d) presents the results, and we observe that the predominant fibre orientation is perpendicular to the MFD in the core and much more uniform in the two other layers. The noise in the measurements is probably explained by the relatively low number of fibres included in the analysis of each layer. Note that the tendency of alignment with the MFD increases slightly with the distance from the core, as previously indicated by the orientation tensor components. We also observe that the global FOD in the *xy*-plane for the entire volume is nearly random despite the through-thickness variation of fibre orientations.

Fig. 3(a) shows FODs for the scanned volume of PA30. Here, we observe that the mean projected fibre orientation in all planes is 0°. Again, the distributions in the *xz*- and *yz*-plane are relatively narrow, which implies that the out-of-plane component is generally small and that the probability of large out-of-plane angles is very low. In the plate plane, however, all fibre angles are well represented and we observe a minor and major peak, respectively, for fibre angles transverse and along the MFD. The orientation tensor components O_{xx} and O_{yy} in Fig. 3(b) indicate that the degree of alignment in the MFD is high close to the surfaces and decreases rather rapidly when approaching the core layer, where the fibre alignment is perpendicular to the MFD. This tendency is much more pronounced for PA30 than for PA15. Again, the out-of-plane component O_{zz} is negligible. Fig. 3(b) shows also that the fibre content in the core is approximately twice as high as in the shell layers. This observation is in accordance with findings reported by Rolland et al. [7] and Sun et al. [55]. By defining the core layer thickness as the region where $O_{yy}(z) > O_{xx}(z)$, the core layer measures 515 μm, corresponding to 17% of the total plate thickness. The FODs in the *xy*-plane of PA30 are computed for the ROIs illustrated in Fig. 3(c) and the results are presented in Fig. 3(d). A bell-shaped distribution centred at ±90° (perpendicular to the MFD) is observed in the core layer, while almost random fibre orientations are found in the transition regions on both sides of the core (Layer 1). The mean fibre orientation in Layer 2 through 4 is along the MFD and the degree of alignment with the MFD increases with increasing distance from the core. The contribution from the fibres in the core to the global FOD is substantial due to the relatively large core layer thickness and the high fibre volume fraction in the core. Finally, Fig. 3(e) shows the fibres in the PA30 sample with a colour overlay, where the colour of each fibre corresponds to the projected angle in the *xy*-plane. The layered structure is clearly visible. Clustering of fibres is common both in the shell layers and the core of the PA30 material, a phenomenon which was less frequently observed for PA15. Our observations regarding the fibre orientations for the PA30 are in accordance with studies on similar materials [2,6,7,9–18], while the amount of relevant data for materials with 15 wt.% of fibres is very limited.

The fibre diameters and lengths were estimated from the 3D datasets by manually measuring single fibres with a measurement tool available in ImageJ [56]. The mean diameter of ten random fibres was chosen as a representative value of the fibre diameter, and the result was 13.5 μm and 12.6 μm for PA15 and PA30, respectively. The difference between the two estimated diameters is probably explained by the small sample sizes or differences in contrast in the two datasets. Next, the length of 100 adjacent fibres in one of the shells was measured and the results are presented in Fig. 4. Out-of-plane measurements were unfortunately not available from the applied tool, implying that the registered data are the lengths projected to the *xy*-plane. This will obviously shift the distributions towards shorter lengths, but the effect is probably limited due to the generally small out-of-plane orientation component. The estimated mean fibre length for PA15 and PA30 was 430 μm and 371 μm, respectively, and the corresponding mean fibre aspect ratios are 32 and 29. It is emphasized that the presented diameter and length measurements must be considered as rough estimates due to the small sample sizes and the lack of 3D measurements. The shape of the fibre length distributions in Fig. 4, including the fibre length at the peak, is similar to fibre length distributions found in the literature [2–8].

4. Tensile tests

4.1. Experimental programme

To characterize the anisotropic mechanical behaviour of the materials, tensile tests were performed using specimens extracted at angles θ of 0°, 15°, 30°, 45°, 60°, 75° and 90° relative to the MFD for PA15 and PA30, see Fig. 5. For the unreinforced PA, 0°-, 45°- and 90°-specimens were applied. Generally, three replicate tests were carried out for each combination of material and angle.

4.2. Setup of tension tests

The experimental setup applied in the mechanical tests includes the test rig (Instron 5566 test machine with a 10 kN load cell), test specimen, specimen support, two digital cameras and a few light sources. All tests were performed at room temperature and the crosshead was moved vertically at a constant speed until the specimen fractured.

The deformations of the specimen's surface were measured using the finite element-based digital image correlation (DIC) software *eCorr* [57,58]. A black and white speckle pattern was applied on the specimens prior to testing. The sightlines of the two cameras were directed perpendicularly to each other; Camera 1 towards the wide surface of specimen and Camera 2 towards the through-thickness side. The camera resolution was 34 pixels/mm and 65 pixels/mm for the unreinforced and fibre-reinforced materials, respectively, and a DIC element size around 30×30 pixels^2 was applied for all materials. The reported DIC element strains are logarithmic coordinate strains, where the reference coordinate system is selected such that the local x_1-axis is parallel to the force direction, the local x_2-axis is directed across the width of the specimen, and the x_3-axis is through the thickness of the specimen. It was verified that the longitudinal strain obtained from the two cameras coincides up to maximum force, whereas a small difference of no significance was observed by the end of the tests.

A new tensile test specimen for fibre-reinforced polymers, shown in Fig. 6(a) and (b), was designed from FE simulations and a handful of physical experiments. The specimen is supported by pins to avoid the detrimental moments which may occur for clamped supports, does not require end tabs and is relatively short compared to conventional specimens since the deformations are measured by DIC instead of an extensometer. Numerical simulations demonstrated that a radius of curvature of 40 mm gives a rather small stress concentration at the specimen shoulder without making the specimen impractically long. A similar specimen

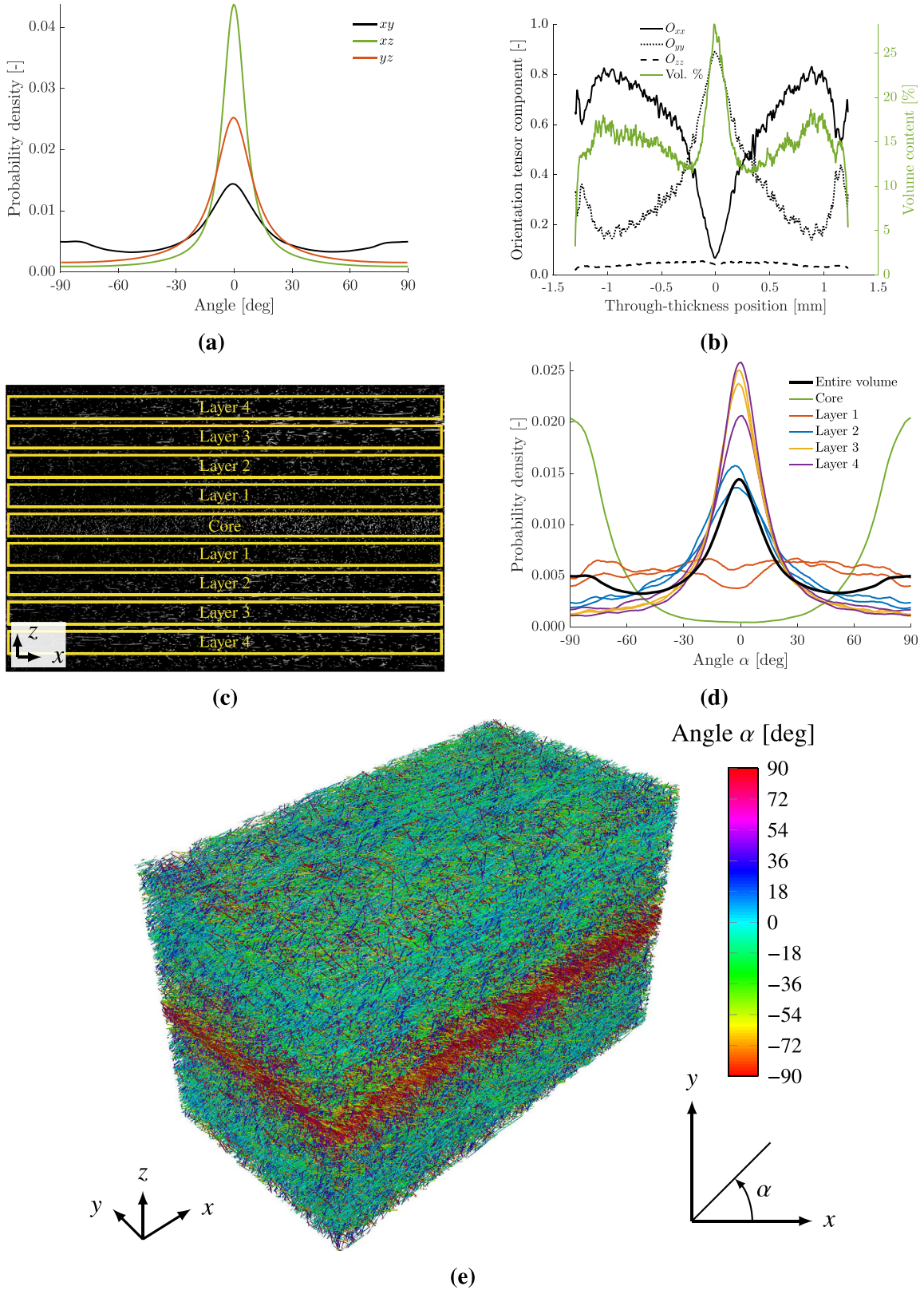

Fig. 3. Quantitative analysis of fibre orientation in PA30. **(a)** Comparison of FODs in the *xy*-, *xz*- and *yz*-plane. **(b)** Orientation tensor components and fibre volume content through the thickness for fibres projected to the *xy*-plane. **(c)** ROIs illustrated in the *xz*-plane. **(d)** FODs in the *xy*-plane for the ROIs. **(e)** Colour overlay of fibre angles when fibres are projected to the *xy*-plane.

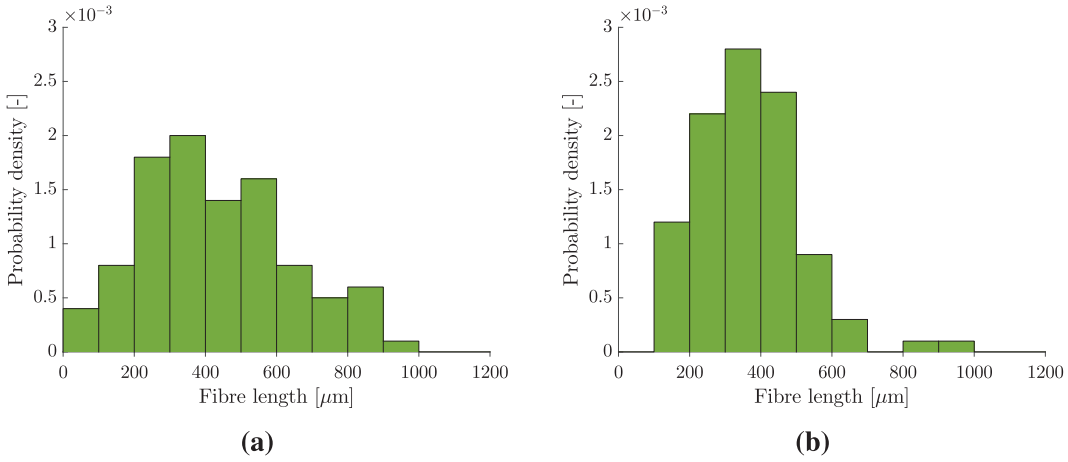

Fig. 4. Fibre length distribution for 100 fibres in one of the shell layers of **(a)** PA15 and **(b)** PA30.

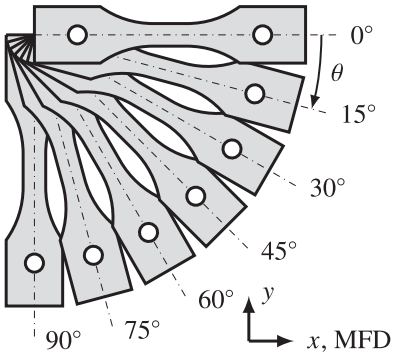

Fig. 5. Definition the specimen orientation angle θ. MFD = Mould Flow Direction and the coordinate system is the same as in Fig. 1.

geometry was applied by Mortazavian and Fatemi [6]. For unreinforced polyamide, it was necessary to strengthen the specimen around the holes by bonding four steel plates to the polymer using a structural adhesive (3M Scotch-Weld DP8805NS), see Fig. 6(c). The surfaces to be bonded were prepared according to the guidelines of the adhesive, and a clamping jig with tightening bolts was used to obtain a uniform pressure on the four steel plates during curing of the adhesive.

Three tensile test specimens with the same material orientation were extracted from each injection-moulded plate. Illustrations of the approximate locations of the specimens are found in the supplementary material. For the reference 0°-direction, however, six specimens were prepared (using two plates). Measurements of the specimen dimensions are reported in the supplementary material. A crosshead velocity of 2.5 mm/min was used in most of the tensile tests, which resulted in measured elastic strain rates in the gauge section of 0.8×10^{-3} s^{-1} for the fibre reinforced material and 1.4×10^{-3} s^{-1} for the unreinforced material. The comparably higher rate is due to the bonded steel plates, which limit the local deformations around the holes of the specimens. Images were acquired at either 5 or 8 frames per second, which for the fibre-reinforced materials typically resulted in between 300 and 600 images from each camera per test.

4.3. Treatment of measured data

The unreinforced PA material deformed homogeneously before the deformation eventually localized and a stable neck was formed. For this material, a representative measure of each strain component was obtained as the mean of the element values in the DIC element row centred in the neck, as demonstrated for Camera 1 in Fig. 7(a).

For the fibre-reinforced materials, however, highly inhomogeneous strain fields developed from early in the tests, as we observe in Fig. 7(b). A few tensile tests without painted surfaces revealed that the inhomogeneities are caused by small cracks in the specimen surfaces, similar to observations presented by Nouri et al. [59]. Furthermore, from around maximum force until the end of the tests, the strain localized in a region of higher strain. To handle both the inhomogeneous strain fields and the localized deformation, the representative value of each

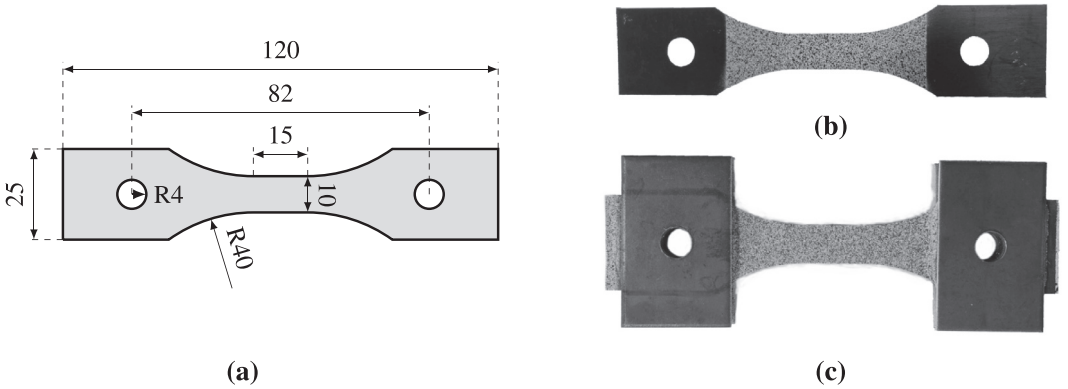

Fig. 6. **(a)** Geometry of the tensile test specimen (dimensions given in mm) and images of the specimens used for the **(b)** fibre-reinforced and **(c)** unreinforced material.

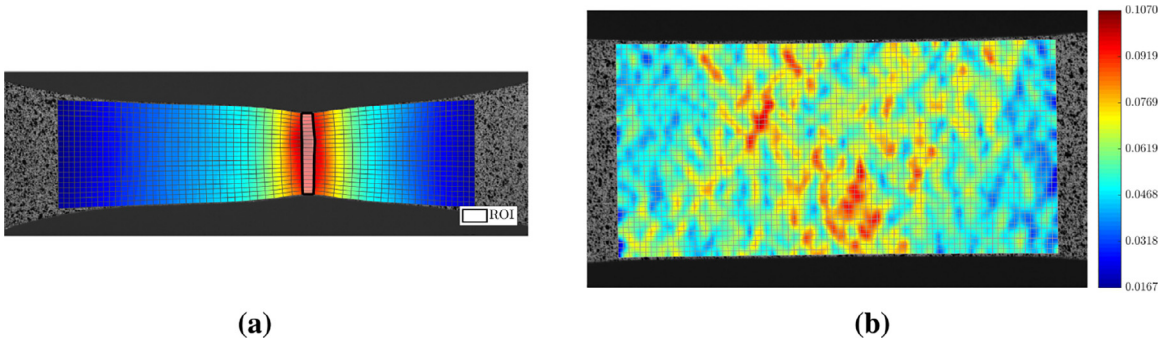

Fig. 7. **(a)** Strain measure and Region Of Interest (ROI) used for tensile tests of unreinforced PA. **(b)** The ε_{11} strain field shortly after maximum force in a tensile test in the 0°-direction of PA15.

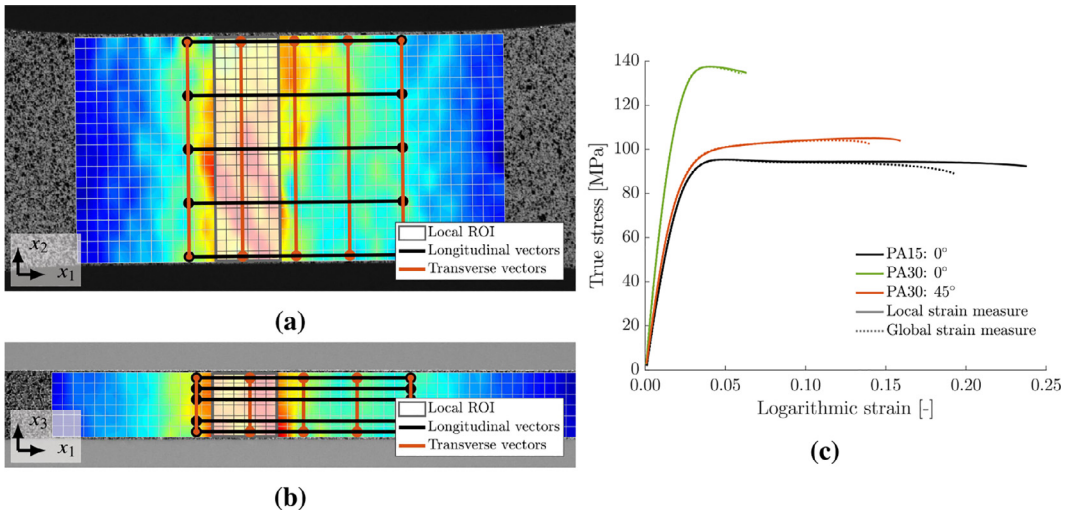

Fig. 8. Illustration of the ROI used in the local strain measure applied in the tensile tests on fibre-reinforced PA and the vectors used to define a comparative global strain measure, shown for the **(a)** wide and **(b)** through-thickness side of the specimen. The element strain values by the end of the test are here plotted for the undeformed configuration (reference image) and the colours blue and red correspond to low and high strain, respectively. **(c)** Comparison of stress-strain curves based on the local and the global strain measures for a few representative tests.

strain component was calculated as the mean element strain within a local region of interest (ROI) with length equal to the specimen thickness, as illustrated in Fig. 8(a) and (b). The ROI was positioned to the region within the gauge section with highest strain and the position was correlated between the two cameras. This strain is thus a local measure of the deformation in the neck. In addition, a global strain measure was defined. The global strain was calculated as the mean logarithmic strain of five parallel vectors in the longitudinal as well as transverse direction, also illustrated in Fig. 8(a) and (b). The global strain measure is compared to the local one in Fig. 8(c). As expected, the two measures coincide up to maximum force, while the local strain measure provides higher strains in the last part of tests where localized deformation occurs. Throughout this work, the local strain measure is applied for the fibre-reinforced materials.

The applied stress measure is true stress, calculated as

$$\sigma = \frac{F}{A} = \frac{F}{w_0 \lambda_2 t_0 \lambda_3} = \frac{F}{A_0 \exp(\varepsilon_{22} + \varepsilon_{33})} \tag{2}$$

where F is the force, A is the current area, A_0 is the initial area, w_0 and t_0 are the initial width and thickness, λ_2 and λ_3 are the stretches in the width and thickness direction, respectively, while ε_{22} and ε_{33} are the synchronized logarithmic transverse strains obtained from the local ROIs defined in Fig. 8. The elastic coefficients, namely Young's modulus E, in-plane Poisson's ratio $\nu_{\text{in-plane}}$ and out-of-plane Poisson's ratio $\nu_{\text{out-of-plane}}$, as well as the elastic strain rate, were computed by performing a linear regression on the relevant response curves within the interval between 10% and 40% of maximum force, for which the response was linear.

4.4. Results and discussion

The stress-strain curves for all tests on unreinforced PA are plotted in Fig. 9(a). The material shows a typical response for thermoplastics, incorporating a well-defined yield point and significant strain hardening. The "knee" of the stress-strain curve corresponds to the local maximum of the measured force, which also coincides with the onset of necking. Some of the tensile tests of unreinforced PA were terminated prior to material failure and the presented curves are therefore cut at a strain equal to 1.0, well beyond relevant strain levels for the fibre-reinforced materials. Although not shown here, the 0°-specimens fractured before the material was cold-drawn contrary to the 45°- and 90°-specimens. The unreinforced PA is clearly an anisotropic material.

Stress-strain curves from the tensile tests on PA15 are plotted in Fig. 9(b). Common to all tests is a linear part followed by a transition region where the tangent modulus is reduced from Young's modulus to zero, which occurs around maximum force, and finally a region of nearly constant stress until fracture. The material is rather ductile for all angles θ and necking is clearly visible before fracture. In the figure, a running average measure is applied to represent the mean behaviour of replicate tests. The measure is obtained by first interpolating the stress-strain curves to a linearly spaced strain vector and then averaging the stress values at each discrete strain value. With this measure, a jump appears

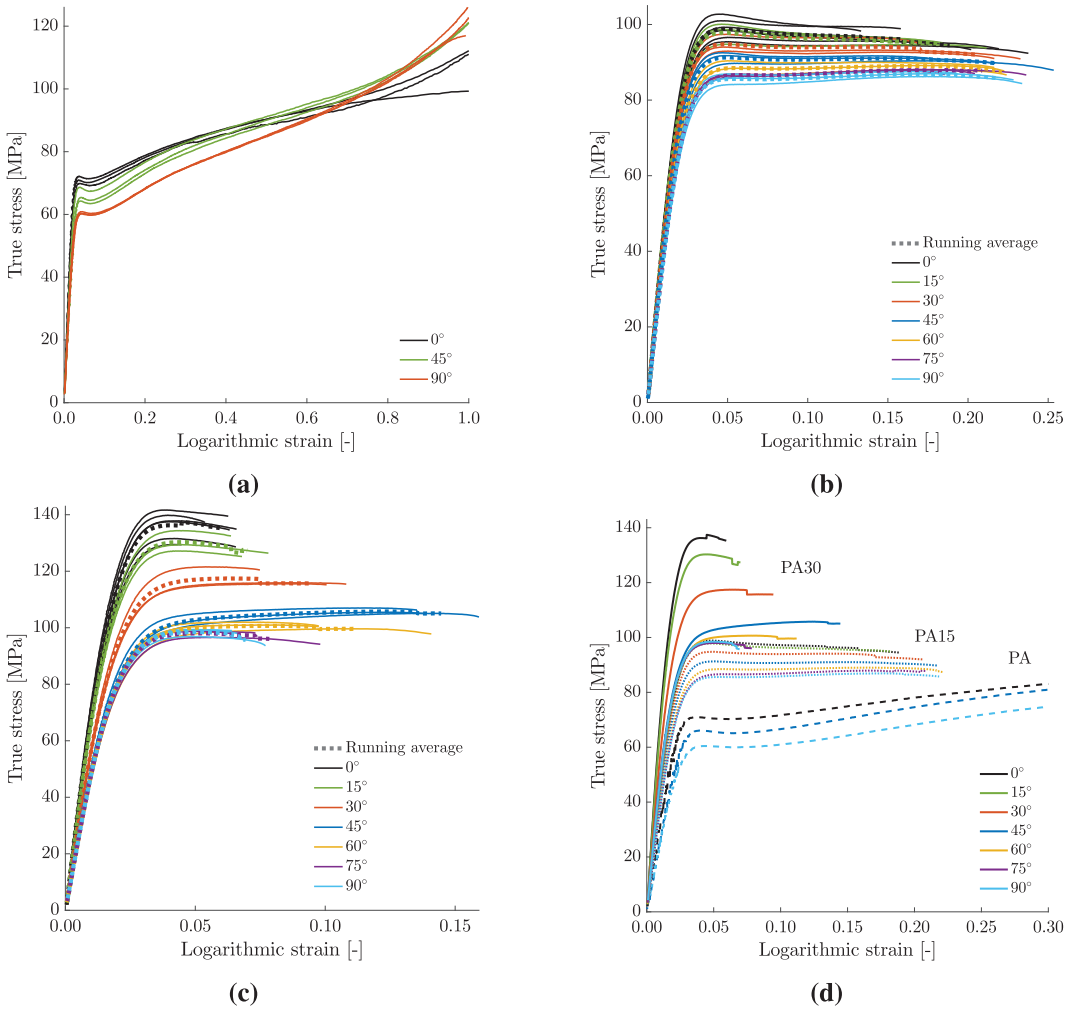

Fig. 9. Stress–strain curves from tensile tests of **(a)** PA (cut at a strain equal to 1.0), **(b)** PA15 and **(c)** PA30, whereas **(d)** compares the running averages of the stress-strain curves for the three materials. The specimen angles are defined in Fig. 5(a).

when one of replicate tests ends, and the ultimate strain of the running average measure is selected as the mean ultimate strain of the replicate tests. Fig. 9(c) plots the stress-strain curves for PA30 and we observe curves with similar shape as described for PA15, except for a more pronounced anisotropy and much larger variation in ultimate strain with the specimen angle.

Fig. 9(d) compares the running averages of the stress-strain curves for PA, PA15 and PA30. As expected, increasing the fibre content increases the stiffness and maximum stress and reduces the ductility of the material. Furthermore, it is clear that the anisotropy increases with the amount of glass fibres. This is also expected, both since increasing the fraction of fibres, which are anisotropic by nature, will increase the anisotropy of the composite material and because the FOD of PA30 is highly non-uniform (Fig. 3(d)) unlike the FOD of PA15 (Fig. 2(d)). PA15 and PA30 show nearly constant stress levels after maximum force until fracture, despite the substantial strain hardening observed above 7% strain for the matrix material. This suggests that, in the region of nearly constant stress, the softening caused by damage in the composite materials approximately levels out the hardening provided by the matrix material. Also, the local strain measure applied in this work promotes a true stress level that exhibits less softening than observed in previous studies [2,6,22,23].

Fig. 10 plots the elastic coefficients from the tensile tests of PA, PA15 and PA30 as function of specimen orientation, where the mean values of the presented data are given in Table 3. According to Fig. 10(a), Young's

Table 3
Mean values of Young's modulus E, stress at maximum force σ_{Fmax}, ultimate strain ϵ_{ult}, in-plane Poisson's ratio $\nu_{\text{in-plane}}$ and out-of-plane Poisson's ratio $\nu_{\text{out-of-plane}}$ from the tensile tests of PA, PA15 and PA30.

Material	θ [deg]	E [MPa]	σ_{Fmax} [MPa]	ϵ_{ult} [–]	$\nu_{\text{in-plane}}$ [–]	$\nu_{\text{out-of-plane}}$ [–]
PA	0	3106	70.9		0.38	0.37
	45	2531	66.0		0.34	0.41
	90	2497	60.3		0.31	0.46
PA15	0	4558	98.7	0.188	0.41	0.42
	15	4565	97.7	0.183	0.42	0.44
	30	4394	94.6	0.206	0.40	0.46
	45	4273	91.2	0.218	0.39	0.40
	60	3970	88.2	0.221	0.34	0.46
	75	3879	86.4	0.209	0.33	0.50
	90	3838	85.5	0.218	0.32	0.48
PA30	0	7319	136.2	0.059	0.41	0.39
	15	7006	130.2	0.070	0.41	0.45
	30	5902	116.7	0.094	0.42	0.41
	45	5122	103.1	0.145	0.41	0.42
	60	4987	99.8	0.112	0.33	0.43
	75	4974	97.8	0.078	0.25	0.50
	90	4967	98.3	0.069	0.23	0.53

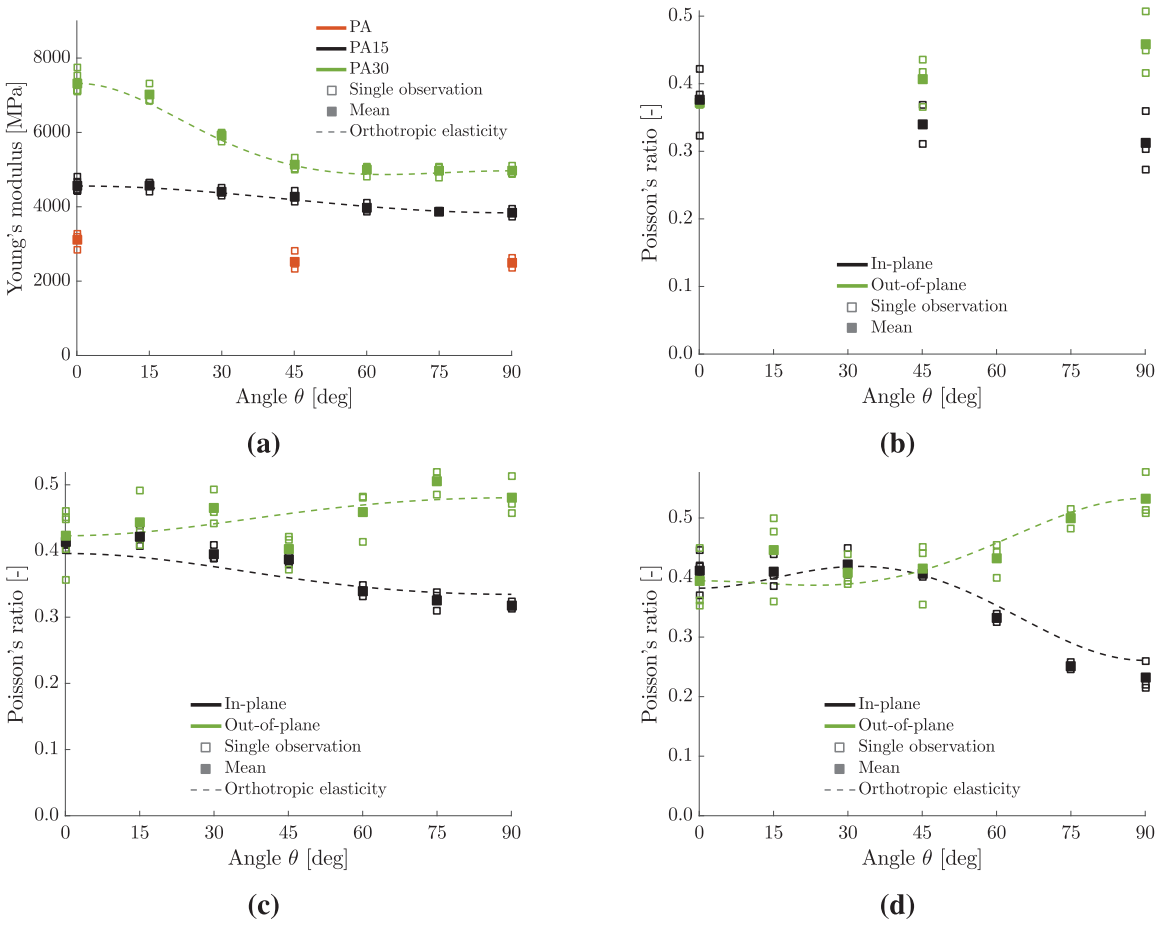

Fig. 10. **(a)** Young's modulus E for all materials. In-plane and out-of-plane Poisson's ratio, $\nu_{\text{in-plane}}$ and $\nu_{\text{out-of-plane}}$, for **(b)** PA, **(c)** PA15 and **(d)** PA30. Mean values of the plotted quantities are given in Table 3.

Table 4
Calibrated engineering constants of orthotropic elasticity for PA15 and PA30.

Material	E_1 [MPa]	E_2 [MPa]	E_3 [MPa]	ν_{12} [–]	ν_{23} [–]	ν_{31} [–]	G_{12} [MPa]	G_{23} [MPa]	G_{31} [MPa]
PA15	4558	3838	4198	0.40	0.48	0.39	1540	1334	1334
PA30	7319	4967	6143	0.38	0.53	0.33	1820	1475	1475

modulus is generally highest for the 0°-direction and lowest for the 90°-direction. For the fibre-reinforced materials, similar values are seen between 45° and 90°, and the evolution for increasing specimen angles follows the general trend typical for this material class [6,9]. Fig. 10(a) also presents Young's modulus of orthotropic elasticity calibrated for PA15 and PA30, a topic which is further discussed shortly.

Fig. 10(b), (c) and (d) show that all materials PA, PA15 and PA30 display large variation in Poisson's ratio with specimen angle. The general trend is that in-plane values decrease and out-of-plane values increase for increasing specimen angles, but this effect is smaller for the less anisotropic material PA15 compared to PA30. For PA30, the predominant fibre orientation is along the MFD and, as expected, a substantially lower in-plane Poisson's ratio is measured for the 90° specimens compared to the 0° specimens. Recall that the classic bounds for Poisson's ratio $-1 < \nu < 0.5$ are limited to isotropic materials and that the values exceeding these limits may be physically admissible for anisotropic materials.

Orthotropic elasticity was calibrated for PA15 and PA30 using the procedure explained in Appendix B, and the values of the calibrated elastic constants are given in Table 4. Fig. 10(a), (c) and (d) compare orthotropic elasticity with experimental data, where Eqs. (B.4), (B.5) and (B.6) are used to plot the elastic coefficients as function of pull direction. We observe that orthotropic elasticity indeed is a very good approximation for these materials, which is in accordance with findings presented by others [6,9,17]. The results also demonstrate the close link between in-plane and out-of-plane Poisson's ratios, and that orthotropic elasticity captures the behaviour seen in the experiments.

Fig. 11 presents the evolution of transverse strains as retraction ratios, computed as $-\varepsilon_{22}/\varepsilon_{11}$ and $-\varepsilon_{33}/\varepsilon_{11}$ for in-plane and out-of-plane transverse strains, respectively. Results from replicate tests are combined by using the running average measure described earlier, which is defined such that a jump appears whenever one of the replicate tests ends. The main observation from Fig. 11 is that the retraction ratio remains relatively constant throughout the deformation sequence at a value near the Poisson's ratio. This finding may be of practical relevance for the development of material models for short fibre-reinforced polymers. More noise is seen for the out-of-plane measurements than for the in-plane measurements, possibly explained by the difference in ROI size used for the strain measures (see Fig. 7(a) and (b)).

Stress at maximum force σ_{Fmax} is plotted for the three materials in Fig. 12(a), and we observe curves with similar shape as was seen for Young's modulus in Fig. 10(a), where highest values are measured

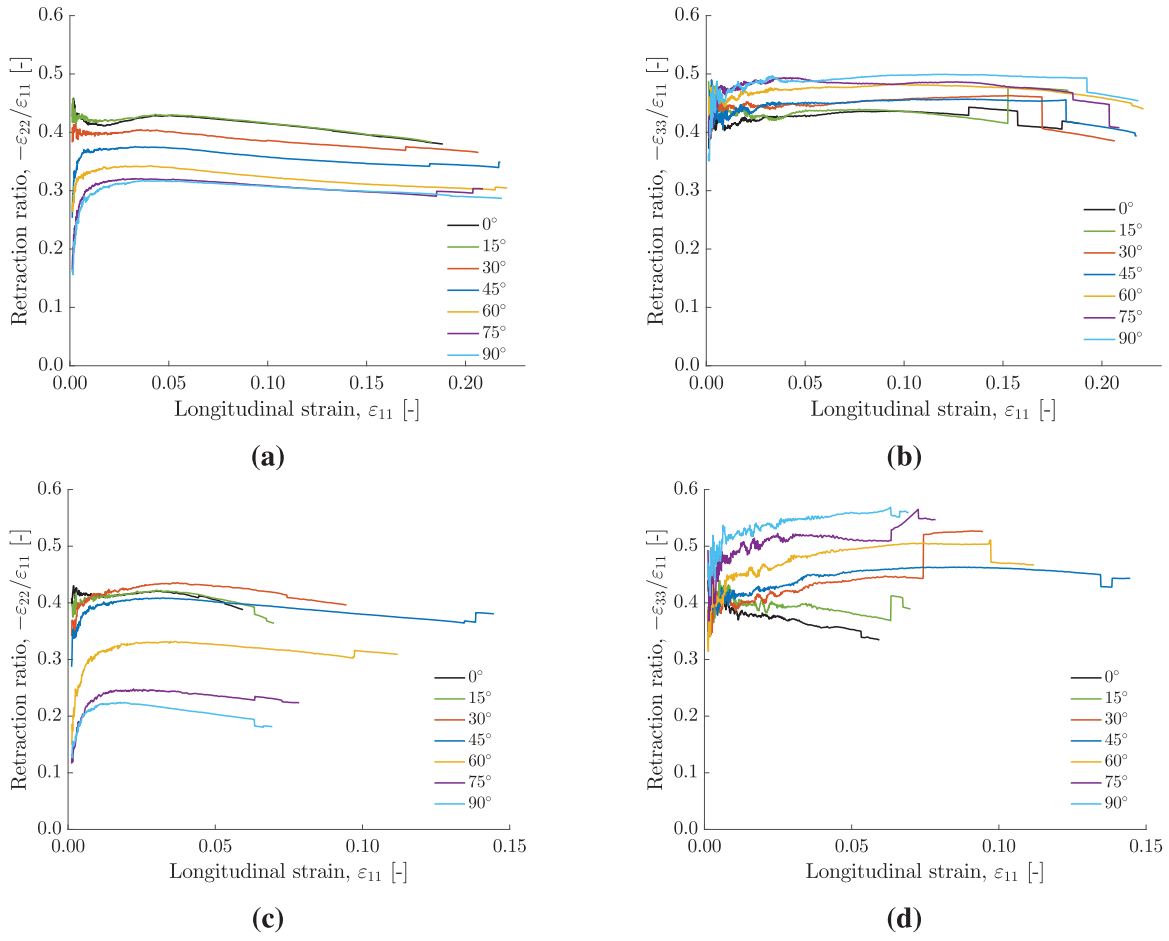

Fig. 11. Evolution of transverse strains as function of longitudinal strain, presented as retraction ratios. **(a)** In-plane, PA15, **(b)** out-of-plane, PA15, **(c)** in-plane, PA30, and **(d)** out-of-plane, PA30.

for 0° specimens and lowest for 90° specimens. Unreinforced PA and PA15, which has a nearly random FOD in the plate plane, show similar anisotropy in measured values of both Young's modulus and stress at maximum force. This indicates that the matrix material contributes to the anisotropy in the composite material and that the contribution may be of the same order of magnitude as the contribution from the fibres when the fibre content is moderate and the degree of fibre alignment with the MFD is small.

Ultimate strain ϵ_{ult} from the tensile tests of PA15 and PA30 is plotted in Fig. 12(b). PA15 fractures at strain around 0.20 for all material orientations, but a weak tendency of increasing ductility with specimen orientation is observed. Note that the scatter in ultimate strain for PA15 is relatively high. For specimen directions 0°, 15° and 30°, the three specimens from each plate are extracted from side-by-side locations (see figure in the supplementary material), and the scatter in the results is at least partly related to the fact that the FOD is not equal in the centre and left/right location of the plates. In fact, for these three specimen directions, the largest values of ultimate strain are from the specimen in the centre. For PA30 we observe that the specimens at the intermediate specimen angles show substantially higher ductility than the 0°- and 90°-specimens, which is a common observation for short fibre-reinforced thermoplastics at similar fibre contents [6,9,10,12,14,22–24]. In Fig. 12(c), the ultimate strains are plotted together with the fibre orientation distributions (plotted as function of θ instead of α). For the materials investigated here, the ultimate strain in a given direction seems to be lower when the amount of glass fibres in this direction is high and vice versa.

Fig. 13 presents contour plots of the coordinate strain ε_{11} (along the pull-direction) at the end of the tests for a selection of representative tests, where the specimens are rotated according to the pull-direction such that the MFD is horizontal for all specimens. Slanted bands of localized deformation are seen for intermediate specimen angles, and the orientation of the bands is close to parallel with the predominant fibre orientation direction, particularly for 45°-specimens. To the authors' best knowledge, such strain fields have not been reported for injection-moulded fibre-reinforced polymers before. Sket et al. [60], however, present similar strain fields for a tensile specimen made of carbon fibres and epoxy resin prepreg sheets (stacking sequence of $[\pm 45^\circ]_{2s}$), and stated that the largest strains were found in a shear band along the fibre direction. Similar results were also reported by Totry et al. [61], who investigated shear stress parallel to the fibres in unidirectional laminates. Both experiments and micro-mechanical simulations showed that shear along the fibres induces localized deformations in a shear band in the matrix, parallel to the fibres. Experimental evidence is also provided by Mortazavian and Fatemi [6], who investigated the off-axis tensile behaviour of a 35 wt.% glass-fibre-reinforced polyamide-6, apparently very similar to the PA30 material used in this work. Scanning electron microscopy (SEM) images of the fracture surfaces showed that brittle matrix fracture occurred in the shells both for 0°- and 90°-specimens. For 45°-specimens, however, significant plastic deformation was observed in the shells parallel to the predominant fibre orientation (along the MFD). Mortazavian and Fatemi [6] suggest that the increased ductility in the 45°-direction is caused by lower constraining effect of the fibres and more pronounced matrix shear band formation.

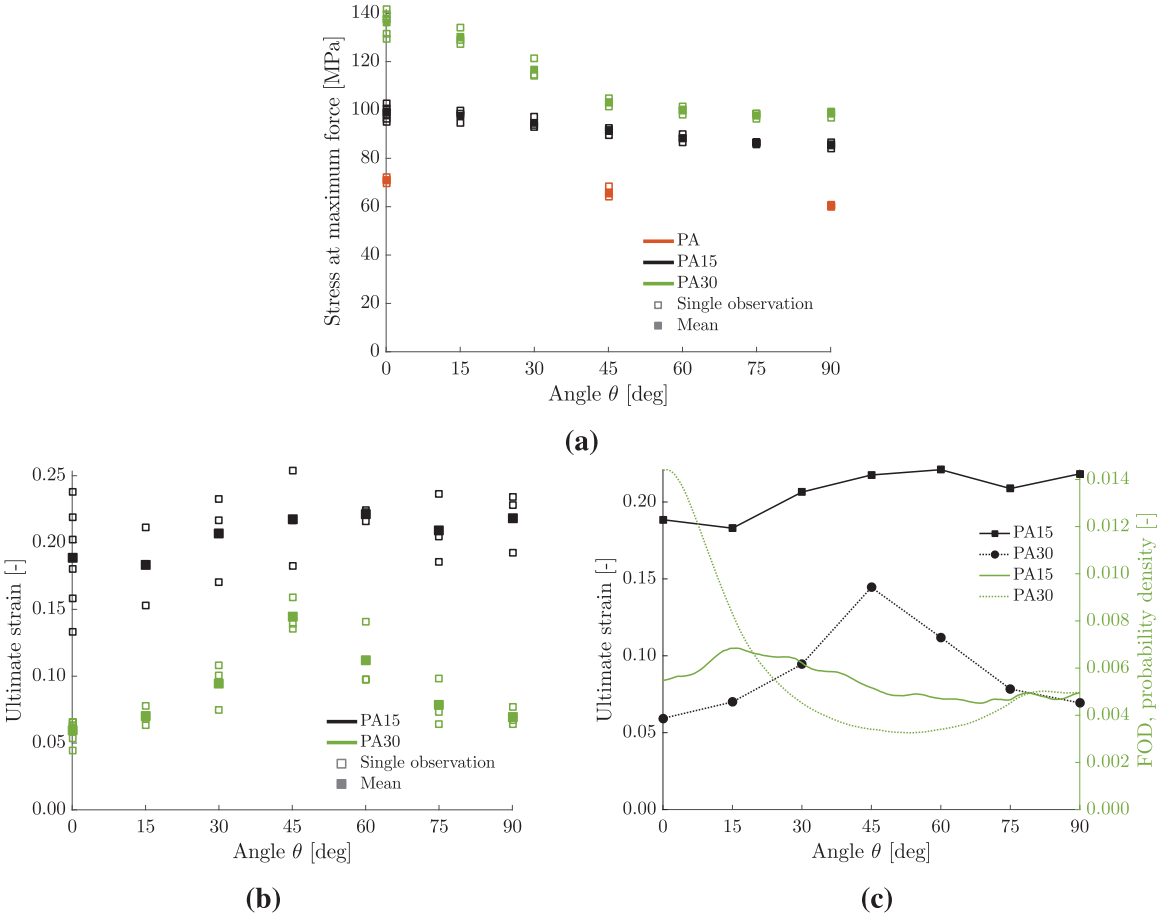

Fig. 12. **(a)** Stress at maximum force σ_{Fmax} and **(b)** ultimate strain ε_{ult}, where the mean values of the plotted quantities are given in Table 3. **(c)** Relation between ultimate strains and the fibre orientation distributions (Fig. 2(a) and 3(a)).

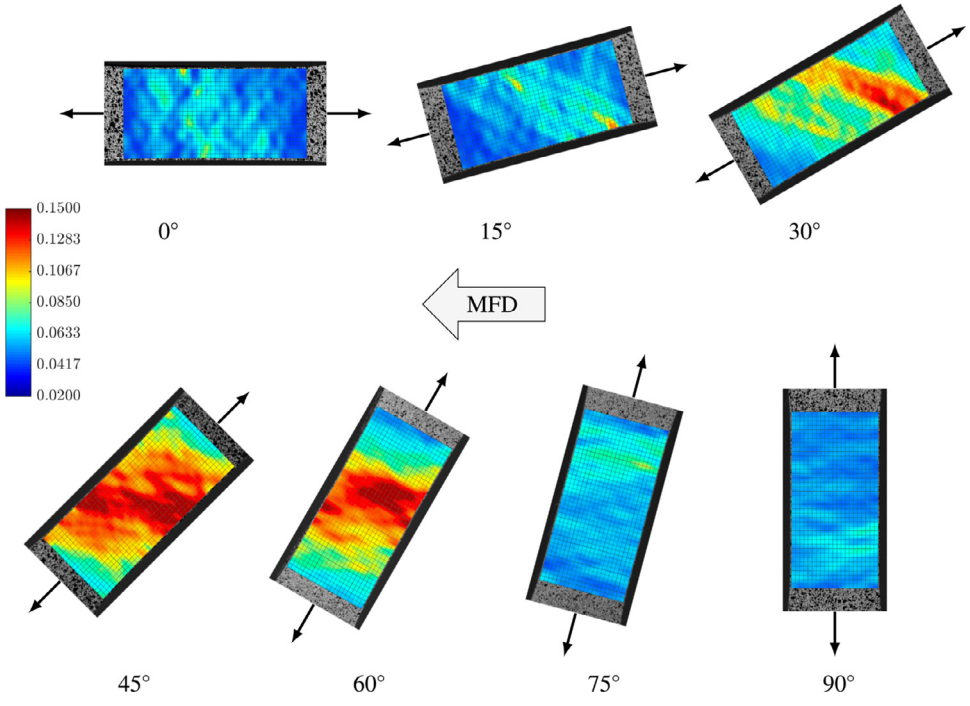

Fig. 13. Contour plots of the coordinate strain ε_{11} (along the pull-direction) immediately before failure for representative tests of PA30. The strain fields are displayed on the reverse side of the specimens compared to Fig. 6(b), which explains why the specimens are rotated counterclockwise.

5. Conclusions

This paper presents an experimental study on the anisotropic tensile behaviour of injection-moulded unreinforced polyamide-6 (PA) and short glass-fibre reinforced polyamide-6 with 15 wt.% (PA15) and 30 wt.% (PA30) fibres. The main findings include:

- *Characterization of the fibre phase*: The fibre-reinforced materials exhibit a three-layered shell-core-shell structure with predominant fibre orientation along and perpendicular to the mould flow direction (MFD) in the shells and core, respectively. The degree of alignment along MFD is largest far from the core and the out-of-plane fibre orientation component is generally small. In average, the FOD in the *xy*-plane for PA15 is nearly uniform, while for PA30, a major peak is present for fibres orientated along the MFD. The fibre volume content is higher in the core layer compared to the shell layers and the thickness of the core layer increases with the fibre content, which makes the core layer more important at higher fibre contents.
- *Off-axis tensile tests*: Instrumentation with two digital cameras facilitates precise measurements of longitudinal strain and both transverse strain components. The use of a local strain measure enables for increased accuracy in reported values of stress and strain. The stiffness and stress at maximum force increase with the fibre content whereas the ductility decreases. For the fibre-reinforced materials, Young's modulus and stress at maximum force are largest in the 0°-direction and tend to decrease as the off-axis angle increases, where similar values are found between 45° and 90°. Generally, the in-plane Poisson's ratio decreases and the out-of-plane value increases for an increasing angle between the tensile axis and the MFD, particularly from 45° to 90°. The transverse strains evolve nearly linearly with the longitudinal strain throughout the deformation sequence. For PA30, the ultimate strain is substantially higher for intermediate specimen angles and the strain fields revealed a slanted region of increased deformation across the specimen, presumably a shear-like deformation mechanism. Results also indicate that when the relative amount of glass fibres in a given direction is high, the ultimate strain in that direction is low and vice versa. PA15 and PA30 are considered to be moderately and highly anisotropic materials, respectively, but the anisotropy of PA15 seems to strongly depend on the anisotropy of the polyamide matrix. Further, it was demonstrated that orthotropic elasticity is an excellent approximation for the fibre-reinforced materials investigated in this work.

Declaration of Competing Interest

The authors declare that they have no known competing financial interests or personal relationships that could have appeared to influence the work reported in this paper.

Acknowledgements

The authors gratefully appreciate the financial support from Centre for Advanced Structural Analysis (CASA) at the Norwegian University of Science and Technology (NTNU), a Centre for Research-based Innovation established by the Research Council of Norway (Project No. 237885). Mr. Trond Auestad and Mr. Tore Wisth at the Structural Impact Laboratory (SIMLab), NTNU, are acknowledged for their invaluable help in the preparation and accomplishment of the experiments.

Appendix A. Supplementary data

Supplementary data for this article is available through Mendeley Data [51], and includes the following: a conversion-equation from fibre weight to fibre volume fraction, measurements of the specimen dimensions, locations of the specimens in the injection-moulded plates and, finally, all plotted data as text files.

Appendix B. Calibration procedure for orthotropic elasticity

We present a calibration procedure of orthotropic elasticity for short fibre-reinforced polymers, which requires 0°, 45° and 90° tensile tests of the fibre-reinforced polymer and one tensile test of the unreinforced polymer. It is assumed that the longitudinal, transverse and through-thickness strains are measured during testing.

Hooke's law (adopting Voigt form) expressed in the principal material coordinate system of an orthotropic elastic material reads (see e.g. [62])

$$\boldsymbol{\sigma} = \boldsymbol{C}\boldsymbol{\varepsilon}$$

$$\begin{bmatrix}\sigma_{11}\\ \sigma_{22}\\ \sigma_{33}\\ \sigma_{23}\\ \sigma_{31}\\ \sigma_{12}\end{bmatrix} = \begin{bmatrix}\frac{1}{E_1} & -\frac{\nu_{21}}{E_2} & -\frac{\nu_{31}}{E_3} & 0 & 0 & 0\\ -\frac{\nu_{12}}{E_1} & \frac{1}{E_2} & -\frac{\nu_{32}}{E_3} & 0 & 0 & 0\\ -\frac{\nu_{13}}{E_1} & -\frac{\nu_{23}}{E_2} & \frac{1}{E_3} & 0 & 0 & 0\\ 0 & 0 & 0 & \frac{1}{G_{23}} & 0 & 0\\ 0 & 0 & 0 & 0 & \frac{1}{G_{31}} & 0\\ 0 & 0 & 0 & 0 & 0 & \frac{1}{G_{12}}\end{bmatrix}^{-1}\begin{bmatrix}\varepsilon_{11}\\ \varepsilon_{22}\\ \varepsilon_{33}\\ \gamma_{23}\\ \gamma_{31}\\ \gamma_{12}\end{bmatrix} \tag{B.1}$$

where $\boldsymbol{\sigma}$ and $\boldsymbol{\varepsilon}$ are the stress and strain vector, respectively, and $\boldsymbol{C}$ is the stiffness matrix, which is the inverse of the compliance matrix $\boldsymbol{S}$, i.e. $\boldsymbol{S} = \boldsymbol{C}^{-1}$. The engineering constants of orthotropic elasticity are E_1, E_2, E_3, ν_{12}, ν_{21}, ν_{23}, ν_{32}, ν_{31}, ν_{13}, G_{12}, G_{23} and G_{31}, where symmetry of the compliance matrix implies the relationships

$$\frac{\nu_{12}}{E_1} = \frac{\nu_{21}}{E_2}, \qquad \frac{\nu_{13}}{E_1} = \frac{\nu_{31}}{E_3}, \qquad \frac{\nu_{23}}{E_2} = \frac{\nu_{32}}{E_3} \tag{B.2}$$

We now consider the orthotropic elastic material in a coordinate system rotated with angle α about the x_3-axis, as illustrated in Fig. B1. The inverse of Hooke's law (on Voigt form) then takes the following form

$$\bar{\boldsymbol{\varepsilon}} = \bar{\boldsymbol{S}}\bar{\boldsymbol{\sigma}}$$

$$\begin{bmatrix}\bar{\varepsilon}_{11}\\ \bar{\varepsilon}_{22}\\ \bar{\varepsilon}_{33}\\ \bar{\gamma}_{23}\\ \bar{\gamma}_{31}\\ \bar{\gamma}_{12}\end{bmatrix} = \begin{bmatrix}\bar{S}_{11} & \bar{S}_{12} & \bar{S}_{13} & 0 & 0 & \bar{S}_{16}\\ \bar{S}_{21} & \bar{S}_{22} & \bar{S}_{23} & 0 & 0 & \bar{S}_{26}\\ \bar{S}_{31} & \bar{S}_{32} & \bar{S}_{33} & 0 & 0 & \bar{S}_{36}\\ 0 & 0 & 0 & \bar{S}_{44} & \bar{S}_{45} & 0\\ 0 & 0 & 0 & \bar{S}_{54} & \bar{S}_{55} & 0\\ \bar{S}_{61} & \bar{S}_{62} & \bar{S}_{63} & 0 & 0 & \bar{S}_{66}\end{bmatrix}\begin{bmatrix}\bar{\sigma}_{11}\\ \bar{\sigma}_{22}\\ \bar{\sigma}_{33}\\ \bar{\sigma}_{23}\\ \bar{\sigma}_{31}\\ \bar{\sigma}_{12}\end{bmatrix} \tag{B.3}$$

where $\bar{\boldsymbol{\varepsilon}}$ and $\bar{\boldsymbol{\sigma}}$ are the strains and stresses expressed in the rotated coordinate system and $\bar{\boldsymbol{S}}$ is the corresponding compliance matrix which relates $\bar{\boldsymbol{\varepsilon}}$ and $\bar{\boldsymbol{\sigma}}$ (see Nemeth [63] or Holmström [64] for details of the derivation). The elements of $\bar{\boldsymbol{S}}$ are listed in Table B1, and may e.g. be used for plotting the engineering constants as function of the angle α.

Table B2 summarizes the applied procedure for calibration of the engineering constants of orthotropic elasticity for short fibre-reinforced polymers, and we will in the following discuss some of the choices made.

E_1, E_2, ν_{12}, ν_{21}, ν_{23} and ν_{13} may be calibrated directly from the results of the 0° and 90° tensile tests of the fibre-reinforced material. The value of ν_{12} should, however, be slightly adjusted to fulfil the over-determined equation $\nu_{12}/E_1 = \nu_{21}/E_2$ in an optimal way.

Next, we will derive an expression for calibration for the G_{12}-value. Coordinate transformations are applied to express the shear strain in the

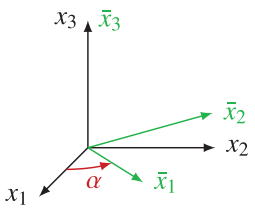

Fig. B1. In-plane coordinate transformation applied to an orthotropic elastic material, where the principal material coordinate system (black) coincides with the global coordinate system and the rotated coordinate system (green) is marked in with an overbar.

Table B1
Elements of the compliance matrix $\bar{S}$ in Eq. (B.3) of an orthotropic elastic material expressed in the coordinate system defined by α in Fig. B1. The elements S_{ij} are given in Eq. (B.1), where symmetry implies $\bar{S}_{ij} = \bar{S}_{ji}$, and $c = \cos(\alpha)$ and $s = \sin(\alpha)$.

$\bar{S}_{11} = \frac{1}{\bar{E}_1}$	$= c^4 S_{11} + s^4 S_{22} + c^2 s^2 (2S_{12} + S_{66})$ $= \frac{c^4}{E_1} + \frac{s^4}{E_2} + c^2 s^2 \left(\frac{1}{G_{12}} - 2\frac{\nu_{12}}{E_1} \right)$	(B.4)
$\bar{S}_{12} = -\frac{\bar{\nu}_{21}}{\bar{E}_2} = -\frac{\bar{\nu}_{12}}{\bar{E}_1}$	$= (c^4 + s^4) S_{12} + c^2 s^2 (S_{11} + S_{22} - S_{66})$ $= c^2 s^2 \left(\frac{1}{E_1} + \frac{1}{E_2} - \frac{1}{G_{12}} \right) - (c^4 + s^4) \frac{\nu_{12}}{E_1}$	(B.5)
$\bar{S}_{13} = -\frac{\bar{\nu}_{31}}{\bar{E}_3} = -\frac{\bar{\nu}_{13}}{\bar{E}_1}$	$= c^2 S_{13} + s^2 S_{23} = -c^2 \frac{\nu_{13}}{E_1} - s^2 \frac{\nu_{23}}{E_2}$	(B.6)
$\bar{S}_{16}$	$= cs(c^2 - s^2)(2S_{12} + S_{66}) + 2cs(s^2 S_{22} - c^2 S_{11})$ $= cs\left[(c^2 - s^2) \left(\frac{1}{G_{12}} - 2\frac{\nu_{12}}{E_1} \right) + 2\left(\frac{s^2}{E_2} - \frac{c^2}{E_1} \right) \right]$	(B.7)
$\bar{S}_{22} = \frac{1}{\bar{E}_2}$	$= s^4 S_{11} + c^4 S_{22} + c^2 s^2 (2S_{12} + S_{66})$ $= \frac{s^4}{E_1} + \frac{c^4}{E_2} + c^2 s^2 \left(\frac{1}{G_{12}} - 2\frac{\nu_{12}}{E_1} \right)$	(B.8)
$\bar{S}_{23} = -\frac{\bar{\nu}_{32}}{\bar{E}_3} = -\frac{\bar{\nu}_{23}}{\bar{E}_2}$	$= c^2 S_{23} + s^2 S_{13} = -c^2 \frac{\nu_{23}}{E_2} - s^2 \frac{\nu_{13}}{E_1}$	(B.9)
$\bar{S}_{26}$	$= cs(s^2 - c^2)(2S_{12} + S_{66}) + 2cs(c^2 S_{22} - s^2 S_{11})$ $= cs\left[(s^2 - c^2) \left(\frac{1}{G_{12}} - 2\frac{\nu_{12}}{E_1} \right) + 2\left(\frac{c^2}{E_2} - \frac{s^2}{E_1} \right) \right]$	(B.10)
$\bar{S}_{33} = \frac{1}{\bar{E}_3}$	$= S_{33} = \frac{1}{E_3}$	(B.11)
$\bar{S}_{36}$	$= 2cs(S_{23} - S_{13}) = 2cs\left(\frac{\nu_{13}}{E_1} - \frac{\nu_{23}}{E_2} \right)$	(B.12)
$\bar{S}_{44} = \frac{1}{\bar{G}_{23}}$	$= c^2 S_{44} + s^2 S_{55} = \frac{c^2}{G_{23}} + \frac{s^2}{G_{31}}$	(B.13)
$\bar{S}_{45}$	$= cs(S_{44} - S_{55}) = cs\left(\frac{1}{G_{23}} - \frac{1}{G_{31}} \right)$	(B.14)
$\bar{S}_{55} = \frac{1}{\bar{G}_{31}}$	$= s^2 S_{44} + c^2 S_{55} = \frac{s^2}{G_{23}} + \frac{c^2}{G_{31}}$	(B.15)
$\bar{S}_{66} = \frac{1}{\bar{G}_{12}}$	$= 4c^2 s^2 (S_{11} + S_{22} - 2S_{12}) + (c^2 - s^2)^2 S_{66}$ $= 4c^2 s^2 \left(\frac{1}{E_1} + \frac{1}{E_2} + 2\frac{\nu_{12}}{E_1} \right) + (c^2 - s^2)^2 \frac{1}{G_{12}}$	(B.16)

Table B2
Applied calibration procedure for the engineering constants of orthotropic elasticity.

Constant	Calibration experiment	Calibration equation
E_1	0°	$E_1 = \frac{\sigma_{11}}{\varepsilon_{11}}$
ν_{12}	0°	$\nu_{12} = -\frac{\varepsilon_{22}}{\varepsilon_{11}}$
ν_{13}	0°	$\nu_{13} = -\frac{\varepsilon_{33}}{\varepsilon_{11}}$
E_2	90°	$E_2 = \frac{\sigma_{22}}{\varepsilon_{22}}$
ν_{21}	90°	$\nu_{21} = -\frac{\varepsilon_{11}}{\varepsilon_{22}}$
ν_{23}	90°	$\nu_{23} = -\frac{\varepsilon_{33}}{\varepsilon_{22}}$
G_{12}	45°	$G_{12} = \frac{\sigma_{12}}{\gamma_{12}} = \frac{\bar{E}_{1,45°}}{2(1+\bar{\nu}_{12,45°})}$
E_3	Assumed values	$E_3 = 0.5(E_1 + E_2)$
G_{31}		$G_{31} = 0.5(G_{\text{matrix}} + G_{12})$
G_{23}		$G_{23} = 0.5(G_{\text{matrix}} + G_{12})$
ν_{31}		$\nu_{31} = \nu_{13} \frac{E_3}{E_1}$
ν_{32}		$\nu_{32} = \nu_{23} \frac{E_3}{E_2}$

principal material coordinate system, γ_{12}, as function of the strains in the local coordinate coordinate system of a test (see e.g. [64] for the derivation),

$$\gamma_{12} = \bar{\gamma}_{12}\left(\cos^2(\alpha) - \sin^2(\alpha)\right) + 2\cos(\alpha)\sin(\alpha)\bar{\varepsilon}_{11} - 2\cos(\alpha)\sin(\alpha)\bar{\varepsilon}_{22} \quad \text{(B.17)}$$

where α refer to Fig. B1. Note that for the particular choice of $\alpha = 45°$, this expression reduces to $\gamma_{12} = \bar{\varepsilon}_{11,45°} - \bar{\varepsilon}_{22,45°}$. A corresponding expression is obtained for the shear stress σ_{12} as

$$\sigma_{12} = \bar{\sigma}_{12}\left(\cos^2(\alpha) - \sin^2(\alpha)\right) + \cos(\alpha)\sin(\alpha)\bar{\sigma}_{11} - \cos(\alpha)\sin(\alpha)\bar{\sigma}_{22} \quad \text{(B.18)}$$

A tensile test has (at least ideally) boundary conditions $\bar{\sigma}_{11} \neq 0$ and $\bar{\sigma}_{22} = \bar{\sigma}_{12} = 0$, which for $\alpha = 45°$ gives $\sigma_{12} = \bar{\sigma}_{11,45°}/2$ from Eq. (B.18) and $\bar{\sigma}_{11,45°} = \bar{E}_{1,45°}\bar{\varepsilon}_{11,45°}$ from Eq. (B.3). In the principal material coordinate system, there is no coupling between shear and normal stresses and Hooke's law gives us the relation $G_{12} = \sigma_{12}/\gamma_{12}$. By inserting the expressions for γ_{12} and σ_{12} from Eqs. (B.17) and (B.18), we obtain an expression for G_{12} as

$$G_{12} = \frac{\sigma_{12}}{\gamma_{12}} = \frac{\bar{E}_{1,45°}\bar{\varepsilon}_{11,45°}}{2(\bar{\varepsilon}_{11,45°} - \bar{\varepsilon}_{22,45°})} = \frac{\bar{E}_{1,45°}}{2(1 + \bar{\nu}_{12,45°})} \quad \text{(B.19)}$$

Values for the engineering constants E_3, G_{31} and G_{23} are not possible to obtain from in-plane tensile tests and little relevant information is available in the literature. Results from a study presented by Ayadi et al. [17] indicate, however, that E_3 is closer to E_1 than to E_2 for an injection-moulded fibre-reinforced polyamide, apparently very similar to the materials investigated in this work. Based on this, it is here assumed that $E_3 = 0.5(E_1 + E_2)$. The expression for G_{12} in Eq. (B.19) demonstrates that the shear modulus in a given plane is highly dependent on Young's modulus in 45° of that plane, which again depends on the amount of fibres around this direction. The FODs for fibres projected to the three coordinate planes, presented in Figs. 2(a) and 3(a), show a significantly lower fraction of fibres oriented at angles around ±45° in the *xz*- and *yz*-plane compared to in the *xy*-plane. The corresponding planes in the coordinate system in Fig. B1 are the 31-, 23- and 12-plane. Hence, it is expected that the values of G_{31} and G_{23} are similar but lower than G_{12}. A lower bound for the shear modulus of the composite material is, however, the shear modulus of the matrix material, which may be estimated as $G_{\text{matrix}} = 0.5E/(1 + \nu)$ assuming that the matrix material is isotropic. In this work, the values for G_{31} and G_{23} are approximated as the average value of the shear modulus of the matrix material, G_{matrix}, and the calculated shear modulus G_{12} of the composite material.

Supplementary materials

Supplementary material associated with this article can be found, in the online version, at doi:10.1016/j.jcomc.2020.100019.

References

[1] M. Akay, D. Barkley, Fibre orientation and mechanical behaviour in reinforced thermoplastic injection mouldings, J. Mater. Sci. 26 (1991) 2731–2742, doi:10.1007/BF00545562.

[2] A. Bernasconi, P. Davoli, A. Basile, A. Filippi, Effect of fibre orientation on the fatigue behaviour of a short glass fibre reinforced polyamide-6, Int. J. Fatigue 29 (2007) 199–208, doi:10.1016/j.ijfatigue.2006.04.001.

[3] J.K. Jørgensen, E. Andreassen, D. Salaberger, The effect of fiber concentration on fiber orientation in injection molded film gated rectangular plates, Polym. Compos. 40 (2) (2019) 615–629, doi:10.1002/pc.24698.

[4] S.Y. Fu, C.Y. Yue, X. Hu, Y.W. Mai, Characterization of fiber length distribution of short-fiber reinforced thermoplastics, J. Mater. Sci. Lett. 20 (1) (2001) 31–33, doi:10.1023/A:1006750328386.

[5] T. Köpplmayr, I. Milosavljevic, M. Aigner, R. Hasslacher, B. Plank, D. Salaberger, J. Miethlinger, Influence of fiber orientation and length distribution on the rheological characterization of glass-fiber-filled polypropylene, Polym. Test. 32 (3) (2013) 535–544, doi:10.1016/j.polymertesting.2013.02.002.

[6] S. Mortazavian, A. Fatemi, Effects of fiber orientation and anisotropy on tensile strength and elastic modulus of short fiber reinforced polymer composites, Compos. B: Eng. 72 (2015) 116–129, doi:10.1016/j.compositesb.2014.11.041.

[7] H. Rolland, N. Saintier, G. Robert, Damage mechanisms in short glass fibre reinforced thermoplastic during in situ microtomography tensile tests, Compos. B: Eng. 90 (2016) 365–377, doi:10.1016/j.compositesb.2015.12.021.

[8] D. Huang, X. Zhao, Novel modified distribution functions of fiber length in fiber reinforced thermoplastics, Compos. Sci. Technol. 182 (June) (2019) 107749, doi:10.1016/j.compscitech.2019.107749.

[9] M. De Monte, E. Moosbrugger, M. Quaresimin, Influence of temperature and thickness on the off-axis behaviour of short glass fibre reinforced polyamide 6.6 Quasi-static loading, Compos. A: Appl. Sci. Manuf. 41 (7) (2010) 859–871, doi:10.1016/j.compositesa.2010.02.018.

[10] B. Klimkeit, Y. Nadot, S. Castagnet, C. Nadot-Martin, C. Dumas, S. Bergamo, C.M. Sonsino, A. Büter, Multiaxial fatigue life assessment for reinforced polymers, Int. J. Fatigue 33 (6) (2011) 766–780, doi:10.1016/j.ijfatigue.2010.12.004.

[11] M.F. Arif, N. Saintier, F. Meraghni, J. Fitoussi, Y. Chemisky, G. Robert, Multiscale fatigue damage characterization in short glass fiber reinforced polyamide-66, Compos. B: Eng. 61 (2014) 55–65, doi:10.1016/j.compositesb.2014.01.019.

[12] A.M. Hartl, M. Jerabek, P. Freudenthaler, R. Lang, Orientation-dependent compression/tension asymmetry of short glass fiber reinforced polypropylene: Deformation, damage and failure, Compos. A: Appl. Sci. Manuf. 79 (2015) 14–22, doi:10.1016/j.compositesa.2015.08.021.

[13] T.B. Nguyen Thi, M. Morioka, A. Yokoyama, S. Hamanaka, K. Yamashita, C. Nonomura, Measurement of fiber orientation distribution in injection-molded short-glass-fiber composites using X-ray computed tomography, J. Mater. Process. Technol. 219 (2015) 1–9, doi:10.1016/j.jmatprotec.2014.11.048.

[14] V. Müller, B. Brylka, F. Dillenberger, R. Glockner, S. Kolling, T. Böhlke, Homogenization of elastic properties of short-fiber reinforced composites based on measured microstructure data, J. Compos. Mater. 50 (3) (2016) 297–312, doi:10.1177/0021998315574314.

[15] D. Notta-Cuvier, M. Nciri, F. Lauro, R. Delille, F. Chaari, F. Robache, G. Haugou, Y. Maalej, Coupled influence of strain rate and heterogeneous fibre orientation on the mechanical behaviour of short-glass-fibre reinforced polypropylene, Mech. Mater. 100 (2016) 186–197, doi:10.1016/j.mechmat.2016.06.013.

[16] H. Rolland, N. Saintier, P. Wilson, J. Merzeau, G. Robert, In situ X-ray tomography investigation on damage mechanisms in short glass fibre reinforced thermoplastics: Effects of fibre orientation and relative humidity, Compo. B: Eng. 109 (2017) 170–186, doi:10.1016/j.compositesb.2016.10.043.

[17] A. Ayadi, H. Nouri, S. Guessasma, F. Roger, Determination of orthotropic properties of glass fibre reinforced thermoplastics using X-ray tomography and multiscale finite element computation, Compos. Struct. 136 (2016) 635–649, doi:10.1016/j.compstruct.2015.10.041.

[18] P.A. Hessman, T. Riedel, F. Welschinger, K. Hornberger, T. Böhlke, Microstructural analysis of short glass fiber reinforced thermoplastics based on x-ray micro-computed tomography, Compos. Sci. Technol. 183 (April) (2019) 107752, doi:10.1016/j.compscitech.2019.107752.

[19] A. Bernasconi, F. Cosmi, E. Zappa, Combined effect of notches and fibre orientation on fatigue behaviour of short fibre reinforced polyamide, Strain 46 (2010) 435–445, doi:10.1111/j.1475-1305.2009.00667.x.

[20] E. Belmonte, M. De Monte, T. Riedel, M. Quaresimin, Local microstructure and stress distributions at the crack initiation site in a short fiber reinforced polyamide under fatigue loading, Polym. Test. 54 (2016) 250–259, doi:10.1016/j.polymertesting.2016.06.013.

[21] A. Ayadi, H. Nouri, S. Guessasma, F. Roger, Large-Scale X-Ray Microtomography Analysis of Fiber Orientation in Weld Line of Short Glass Fiber Reinforced Thermoplastic and Related Elasticity Behavior, Macromol. Mater. Eng. 301 (8) (2016) 907–921, doi:10.1002/mame.201500463.

[22] S. Kammoun, I. Doghri, L. Adam, G. Robert, L. Delannay, First pseudo-grain failure model for inelastic composites with misaligned short fibers, Compos. A: Appl. Sci. Manuf. 42 (12) (2011) 1892–1902, doi:10.1016/j.compositesa.2011.08.013.

[23] S. Kammoun, I. Doghri, L. Brassart, L. Delannay, Micromechanical modeling of the progressive failure in short glass-fiber reinforced thermoplastics – first Pseudo-Grain Damage model, Compos. A: Appl. Sci. Manuf. 73 (2015) 166–175, doi:10.1016/j.compositesa.2015.02.017.

[24] S. Mortazavian, A. Fatemi, Tensile and fatigue behaviors of polymers for automotive applications, Mater. Werkstofftech. 46 (2) (2015) 204–213, doi:10.1002/mawe.201400376.

[25] S.Y. Fu, B. Lauke, Effects of fiber length and fiber orientation distributions on the tensile strength of short-fiber-reinforced polymers, Compos. Sci. Technol. 56 (2) (1996) 1179–1190, doi:10.1016/S0266-3538(96)00072-3.

[26] S.Y. Fu, B. Lauke, E. Mäder, C.Y. Yue, X. Hu, Tensile properties of short-glass-fiber- and short-carbon-fiber-reinforced polypropylene composites, Compos. A: Appl. Sci. Manuf. 31 (10) (2000) 1117–1125, doi:10.1016/S1359-835X(00)00068-3.

[27] J.L. Thomason, M.A. Vlug, G. Schipper, H.G.L.T. Krikor, Influence of fibre length and concentration on the properties of glass fibre-reinforced polypropylene: Part 3. Strength and strain at failure, Compos. A: Appl. Sci. Manuf. 27 (11) (1996) 1075–1084, doi:10.1016/1359-835X(96)00066-8.

[28] J.L. Thomason, The influence of fibre length and concentration on the properties of glass fibre reinforced polypropylene: 5. Injection moulded long and short fibre PP, Compos. A: Appl. Sci. Manuf. 33 (12) (2002) 1641–1652, doi:10.1016/S1359-835X(02)00179-3.

[29] B. Mouhmid, A. Imad, N. Benseddiq, S. Benmedakhene, A. Maazouz, A study of the mechanical behaviour of a glass fibre reinforced polyamide 6,6: rxperimental investigation, Polym. Test. 25 (4) (2006) 544–552, doi:10.1016/j.polymertesting.2006.03.008.

[30] J.L. Thomason, Structure-property relationships in glass-reinforced polyamide, part 1: the effects of fiber content, Polym. Compos. 27 (5) (2006) 552–562, doi:10.1002/pc.20226.

[31] J.L. Thomason, The influence of fibre length and concentration on the properties of glass fibre reinforced polypropylene: 7. Interface strength and fibre strain in injection moulded long fibre PP at high fibre content, Compos. A: Appl. Sci. Manuf. 38 (1) (2007) 210–216, doi:10.1016/j.compositesa.2006.01.007.

[32] J.L. Thomason, The influence of fibre length, diameter and concentration on the modulus of glass fibre reinforced polyamide 6,6, Compos. A: Appl. Sci. Manuf. 39 (11) (2008) 1732–1738, doi:10.1016/j.compositesa.2008.08.001.

[33] J.L. Thomason, M.A. Vlug, Influence of fibre length and concentration on the properties of glass fibre-reinforced polypropylene: 1. Tensile and flexural modulus, Compos. A: Appl. Sci. Manuf. 27 (6) (1996) 477–484, doi:10.1016/1359-835X(95)00065-A.

[34] A. Güllü, A. Özdemir, E. Özdemir, Experimental investigation of the effect of glass fibres on the mechanical properties of polypropylene (PP) and polyamide 6 (PA6) plastics, Mater. Des. 27 (4) (2006) 316–323, doi:10.1016/j.matdes.2004.10.013.

[35] J.L. Thomason, The influence of fibre properties of the performance of glass-fibre-reinforced polyamide 6,6, Composites Science and Technology 59 (16) (1999) 2315–2328, doi:10.1016/S0266-3538(99)00083-4.

[36] B.N. Nguyen, V. Kunc, An elastic-plastic damage model for long-fiber thermoplastics, Int. J. Damage Mech. 19 (6) (2010) 691–725, doi:10.1177/1056789509338319.

[37] D. Notta-Cuvier, F. Lauro, B. Bennani, R. Balieu, An efficient modelling of inelastic composites with misaligned short fibres, Int. J. Solids Struct. 50 (19) (2013) 2857–2871, doi:10.1016/j.ijsolstr.2013.04.031.

[38] E. Chebbi, M. Wali, F. Dammak, An anisotropic hyperelastic constitutive model for short glass fiber-reinforced polyamide, Int. J. Eng. Sci. 106 (2016) 262–272, doi:10.1016/j.ijengsci.2016.07.003.

[39] L. Schulenberg, T. Seelig, F. Andrieux, D.-Z. Sun, An anisotropic elasto-plastic material model for injection-molded long fiber-reinforced thermoplastics accounting for local fiber orientation distributions, J. Compos. Mater. 51 (14) (2017) 2061–2078, doi:10.1177/0021998316668983.

[40] M. Nciri, D. Notta-Cuvier, F. Lauro, F. Chaari, Y. Maalej, B. Zouari, Viscoelasticviscoplastic model for short-fiber-reinforced composites with complex fiber orientation, Mech. Adv. Mater. Struct. 26 (10) (2019) 842–853, doi:10.1080/15376494.2018.1430264.

[41] M. Schemmann, J. Görthofer, T. Seelig, A. Hrymak, T. Böhlke, Anisotropic mean-field modeling of debonding and matrix damage in SMC composites, Compos. Sci. Technol. 161 (2018) 143–158, doi:10.1016/j.compscitech.2018.03.041.

[42] J. Jansson, T. Gustafsson, K. Salomonsson, J. Olofsson, J. Johansson, P. Appelsved, M. Palm, An anisotropic non-linear material model for glass fibre reinforced plastics, Compos. Struct. 195 (2018) 93–98, doi:10.1016/j.compstruct.2018.04.044.

[43] A. Amiri-Rad, L. Pastukhov, L. Govaert, J. van Dommelen, An anisotropic viscoelastic-viscoplastic model for short-fiber composites, Mech. Mater. 137 (2019) 103141, doi:10.1016/j.mechmat.2019.103141.

[44] A. Dean, N. Grbic, R. Rolfes, B. Behrens, Macro-mechanical modeling and experimental validation of anisotropic, pressure- and temperature-dependent behavior of short fiber composites, Compos. Struct. 211 (2019) 630–643, doi:10.1016/j.compstruct.2018.12.045.

[45] G. He, Y. Liu, D.J. Bammann, D.K. Francis, M.Q. Chandler, M.F. Horstemeyer, A multiphase internal state variable model with rate equations for predicting elastothermoviscoplasticity and damage of fiber-reinforced polymer composites, Acta Mech. 230 (5) (2019) 1745–1780, doi:10.1007/s00707-018-2358-1.

[46] W. Tian, L. Qi, C. Su, J. Zhou, Z. Jing, Numerical simulation on elastic properties of short-fiber-reinforced metal matrix composites: Effect of fiber orientation, Compos. Struct. 152 (2016) 408–417, doi:10.1016/j.compstruct.2016.05.046.

[47] K.P. Babu, P.M. Mohite, C.S. Upadhyay, Development of an RVE and its stiffness predictions based on mathematical homogenization theory for short fibre composites, International Journal of Solids and Structures 130-131 (2018) 80–104, doi:10.1016/j.ijsolstr.2017.10.011.

[48] W. Tian, L. Qi, J. Zhou, J. Guan, Effects of the fiber orientation and fiber aspect ratio on the tensile strength of Csf/Mg composites, Comput. Mater. Sci. 89 (2014) 6–11, doi:10.1016/j.commatsci.2014.03.004.

[49] R. Pietrogrande, P.A. Carraro, M. De Monte, M. Quaresimin, A novel pseudo-grain approach for the estimation of the elastic stress distributions within the matrix of short fiber-reinforced polymers, Compos. B: Eng. 150 (2018) 115–123, doi:10.1016/j.compositesb.2018.05.038.

[50] W. Ogierman, G. Kokot, Generation of the representative volume elements of composite materials with misaligned inclusions, Compos. Struct. 201 (2018) 636–646, doi:10.1016/j.compstruct.2018.06.086.

[51] P.H. Holmström, Data for: anisotropic tensile behaviour of short glass-fibre reinforced polyamide-6, 2020, (Mendeley Data, V1). doi:10.17632/v6jxkjtrt3.1.

[52] S. Mortazavian, A. Fatemi, A. Khosrovaneh, Effect of water absorption on tensile and fatigue behaviors of two short glass fiber reinforced thermoplastics, SAE Int. J. Mater. Manuf. 8 (2) (2015), doi:10.4271/2015-01-0546.

[53] M. Eftekhari, A. Fatemi, Tensile behavior of thermoplastic composites including temperature, moisture, and hygrothermal effects, Polym. Test. 51 (2016) 151–164, doi:10.1016/j.polymertesting.2016.03.011.

[54] S.G. Advani, C.L. Tucker, The use of tensors to describe and predict fiber orientation in short fiber composites, J. Rheol. 31 (1987) 751, doi:10.1122/1.549945.

[55] X. Sun, J. Lasecki, D. Zeng, Y. Gan, X. Su, J. Tao, Measurement and quantitative analysis of fiber orientation distribution in long fiber reinforced part by injection molding, Polym. Test. 42 (2015) 168–174, doi:10.1016/j.polymertesting.2015.01.016.

[56] C.A. Schneider, W.S. Rasband, K.W. Eliceiri, NIH Image to ImageJ: 25 years of image analysis, Nat. Methods 9 (7) (2012) 671–675, doi:10.1038/nmeth.2089.

[57] E. Fagerholt, User manual - eCorr - Digital Image Correlation Tool, 2019. https://www.ntnu.edu/kt/ecorr.

[58] E. Fagerholt, T. Børvik, O.S. Hopperstad, Measuring discontinuous displacement fields in cracked specimens using digital image correlation with mesh adaptation and crack-path optimization, Opt. Lasers Eng. 51 (3) (2013) 299–310, doi:10.1016/j.optlaseng.2012.09.010.

[59] H. Nouri, S. Guessasma, F. Roger, A. Ayadi, H. Maitournam, Exploring damage kinetics in short glass fibre reinforced thermoplastics, Compos. Struct. 180 (2017) 63–74, doi:10.1016/j.compstruct.2017.07.096.

[60] F. Sket, A. Enfedaque, C. Díaz López, C. González, J. Molina-Aldareguía, J. LLorca, X-ray computed tomography analysis of damage evolution in open hole carbon fiber-reinforced laminates subjected to in-plane shear, Compos. Sci. Technol. 133 (2016) 40–50, doi:10.1016/j.compscitech.2016.06.012.

[61] E. Totry, C. González, J. Llorca, J.M. Molina-Aldareguía, Mechanisms of shear deformation in fiber-reinforced polymers: experiments and simulations, Int. J. Fract. 158 (2) (2009) 197–209, doi:10.1007/s10704-009-9353-4.

[62] F. Irgens, Continuum Mechanics, 1st, Springer, 2008.

[63] M.P. Nemeth, An in-depth tutorial on constitutive equations for elastic anisotropic materials, Technical Report, NASA Langley Reseach Center, 2011.

[64] P.H. Holmström, An experimental and numerical study of the mechanical behaviour of short glass-fibre reinforced thermoplastics, Ph.D. thesis, Norwegian University of Science and Technology, 2019.